

# CMOS-compatible photonic integrated circuits on thin-film ScAlN

Sihao Wang,<sup>1, a)</sup> Veerendra Dhyani,<sup>1, a)</sup> Sakthi Sanjeev Mohanraj,<sup>1</sup> Xiaodong Shi,<sup>1</sup> Binni Varghese,<sup>2</sup> Wing Wai Chung,<sup>2</sup> Ding Huang,<sup>1</sup> Zhi Shih Lim,<sup>1</sup> Qibin Zeng,<sup>1</sup> Huajun Liu,<sup>1</sup> Xianshu Luo,<sup>2</sup> Victor Leong,<sup>1</sup> Nanxi Li,<sup>2, b)</sup> and Di Zhu<sup>1, 3, 4, c)</sup>

<sup>1)</sup>*Institute of Materials Research and Engineering (IMRE), Agency for Science, Technology and Research (A\*STAR),*

*2 Fusionopolis Way, Innovis #08-03, Singapore 138634, Republic of Singapore*

<sup>2)</sup>*Institute of Microelectronics (IME), Agency for Science, Technology and Research (A\*STAR),*

*2 Fusionopolis Way, Innovis #08-02, Singapore 138634, Republic of Singapore*

<sup>3)</sup>*Department of Materials Science and Engineering, National University of Singapore, Singapore 117575, Singapore*

<sup>4)</sup>*Centre for Quantum Technologies, National University of Singapore, Singapore 117543, Singapore*

Scandium aluminum nitride (ScAlN) has recently emerged as an attractive material for integrated photonics due to its favorable nonlinear optical properties and compatibility with CMOS fabrication. Despite the promising and versatile material properties, it is still an outstanding challenge to realize low-loss photonic circuits on thin-film ScAlN-on-insulator wafers. Here, we present a systematic study on the material quality of sputtered thin-film ScAlN produced in a CMOS-compatible 200 mm line, and an optimized fabrication process to yield 400 nm thick, fully etched waveguides. With surface polishing and annealing, we achieve micro-ring resonators with an intrinsic quality factor as high as  $1.47 \times 10^5$ , corresponding to a propagation loss of 2.4 dB/cm. These results serve as a critical step towards developing future large-scale, low-loss photonic integrated circuits based on ScAlN.

## I. INTRODUCTION

Photonic integrated circuits (PICs) hold great promise in realizing compact and scalable systems for a wide range of applications, from communications<sup>1,2</sup> and computing<sup>3</sup> to sensing<sup>4</sup> and metrology<sup>5,6</sup>. However, some of them demand functionalities beyond what traditional silicon photonics can offer, such as low-loss electro-optic or acoustic-optic modulation, broadband operation down to visible or ultraviolet (UV) wavelengths, and second-order parametric wavelength conversion. This has motivated the search for integrated photonics materials with more versatile properties.

Aluminum nitride (AlN) has emerged as an attractive candidate<sup>7</sup>. As a material widely used in the Micro-Electro-Mechanical Systems (MEMS)<sup>8</sup>, AlN also shows the potential in areas such as optomechanics<sup>9</sup> and nonlinear optics<sup>10</sup>. It has a wide bandgap of 6.2 eV<sup>11</sup>, allowing operation from deep UV to mid-infrared (MIR)<sup>12</sup>. Already used as an insulator for microelectronic packaging<sup>13,14</sup>, AlN is compatible with complementary metal-oxide semiconductor (CMOS) fabrication processes, making it a promising material for future foundry-level PIC manufacturing.

Theoretical prediction<sup>15–19</sup> of introducing rare-earth dopants for piezoelectricity enhancement has motivated research on doping scandium (Sc) in AlN. It has been demonstrated that the piezoelectric coefficient could be improved by more than 5 times in Sc-doped AlN (ScAlN)<sup>19</sup>. Further investigation of the effect of Sc doping reveals several favorable properties of ScAlN. Sc doping flattens the Gibbs free-energy band structure of the wurtzite AlN, enabling its ferroelectricity<sup>20–22</sup>. This allows ferroelectric domain engineering and periodic poling. The second-order nonlinearity ( $\chi^{(2)}$ ) has been shown to improve with the Sc content<sup>23</sup>. The  $d_{33}$  component in 36% Sc doped AlN is shown

to be one order of magnitude higher than that in the undoped AlN, and also twice of that in lithium niobate (LN). Sc doping is thus a promising strategy to improve the nonlinearity of AlN integrated photonic devices. However, it also introduces losses and makes the material harder to etch. So far, there are very limited studies and successes in achieving low-loss waveguides in ScAlN<sup>23–25</sup>, and few-dB/cm loss is only demonstrated very recently in thin (150 nm) and partially etched (100 nm) ScAlN waveguides, which sacrifices mode confinement in ScAlN<sup>26</sup>.

In this work, we present a systematic study on the fabrication of low-loss ScAlN PIC. We perform a detailed material study on sputter-deposited ScAlN films on 200 mm wafers and develop an optimized fabrication process to produce fully etched waveguides and ring resonators. We illustrate the effect of etching and annealing on the resonator quality factor ( $Q$ ). By thermally healing the ScAlN thin film, we are able to reduce the absorption loss, achieving an average intrinsic  $Q$  over  $1.00 \times 10^5$  (highest at  $1.47 \times 10^5$ , corresponding to 2.4 dB/cm propagation loss). Our result paves a viable path towards the development of future low-loss, large-scale, and multifunctional ScAlN PICs.

## II. METHODS AND RESULTS

The ScAlN thin film is prepared by physical vapour deposition (PVD) on 200-mm Si wafers at the Institute of Microelectronics (IME). A sputtering target of nominal 10% Sc-doped aluminum is used to deposit 500 nm thick ScAlN films on 4  $\mu\text{m}$  thermal oxide-on-silicon substrate. The ScAlN alloy inherits the lattice structure from either AlN or scandium nitride (ScN), depending on the Sc doping concentration. AlN exhibits a stable wurtzite structure (space group  $P6_3mc$ ) with a six-fold in-plane rotation symmetry (point group  $C_{6v}$ ), and is polar along the  $c$ -axis. ScN has a nonpolar stable ground-state rock-salt phase (space group  $Fm\bar{3}m$ , point group  $O_h$ ). Theoretical density functional theory (DFT) of ScAlN<sup>27</sup> predicts a stable wurtzite phase with Sc contents up to 56%, above which the rock salt phase is more favorable. The thin-film sample

<sup>a)</sup>These two authors contributed equally

<sup>b)</sup>Electronic mail: [linx1@ime.a-star.edu.sg](mailto:linx1@ime.a-star.edu.sg)

<sup>c)</sup>Electronic mail: [dizhu@nus.edu.sg](mailto:dizhu@nus.edu.sg)

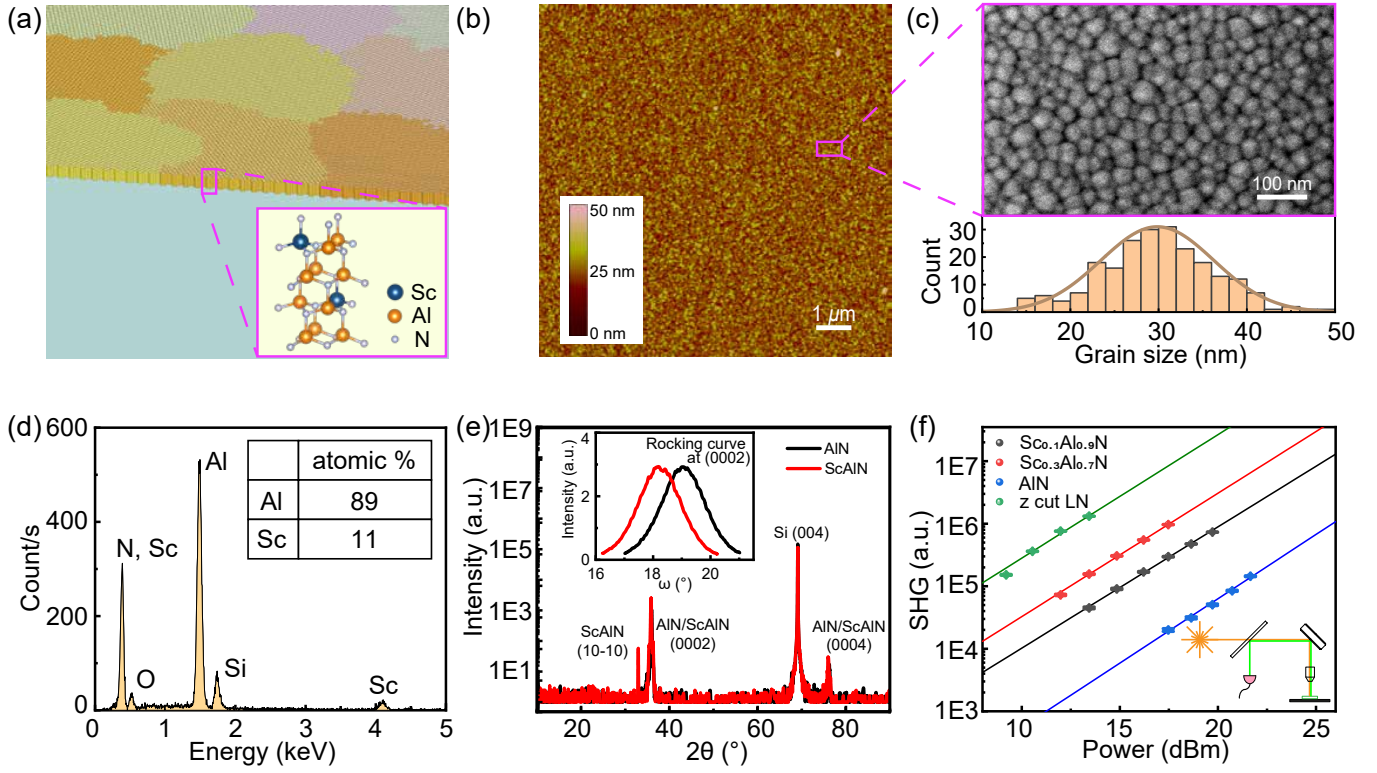


FIG. 1. Material characterization of ScAlN thin films. (a) Illustration of thin-film ScAlN with the  $c$ -axis perpendicular to the surface. The inset shows the lattice structure of ScAlN. (b) AFM image shows the rough surface after sputtering. The RMS surface roughness is 5.2 nm. (c) SEM image of the thin-film surface shows grain-like structure with a mean grain size of 30 nm. The bottom figure is the grain size distribution. (d) EDX measurement shows the relative elemental composition, revealing a 11% doping of scandium. The additional silicon and oxygen are from the HSQ residue. (e) The XRD measurement reveals a single phase of sputtered AlN film with the  $c$ -axis pointing perpendicular to the surface. The additional (10-10) peak from the ScAlN film indicates that the sputtered ScAlN film sees two planes ( $c$  plane and  $m$  plane). The slight down-shift of the peaks reveals the slight expansion of the lattice due to the larger ionic radius of  $\text{Sc}^{3+}$  over  $\text{Al}^{3+}$ . The inset is the rocking curve measurements comparing the sputtered AlN and ScAlN. Both have a FWHM of  $1.8^\circ$ , indicating the presence of the some amorphous parts. (f) A confocal SHG measurement on thin-film samples demonstrates the nonlinear optical effect in ScAlN. Four samples are 10% doped ScAlN( $\text{Sc}_{0.1}\text{Al}_{0.9}\text{N}$ ), 30% doped ScAlN( $\text{Sc}_{0.3}\text{Al}_{0.7}\text{N}$ ), undoped AlN, and z-cut LN. The SHG signal increases with Sc doping concentration. The inset is the schematic of the confocal setup.

grown from a nominal 10% scandium doped target is hence expected to be in wurtzite phase. Fig. 1(a) shows an illustration of ScAlN thin film on thermal oxide. The honeycomb shape represents the hexagonal shape of the wurtzite structure, when being viewed along the  $c$ -axis. The film is polycrystalline with individual domains shown by different colors and orientations. The inset shows a wurtzite structure with the Al atoms being replaced by the Sc dopants. While doping flattens the wurtzite structure towards the layered hexagonal structure<sup>28</sup>, the current ScAlN film is still expected to exhibit a wurtzite structure due to the relatively low doping concentration.

Fig. 1(b) presents an atomic force microscope (AFM) image of an as-grown film, showing a root-mean-square (RMS) surface roughness of 5.2 nm. Congregation of materials forms nanocolumns ranging from <100 nm to 300 nm, evidenced by the bright spots in the AFM image. This length scale is comparable to the photon wavelengths of 1550 nm, implying an additional source of scattering loss. A magnified image from a scanning electron microscope (SEM) in Fig. 1(c) reveals

a granular surface with a mean grain size of 30 nm. This provides an avenue for charge trapping, defect creation and dangling bonds, which are all detrimental to film quality. The grain size distribution is shown in the lower part of Fig. 1(c). An energy-dispersive X-ray spectroscopy (EDX) is performed to identify the elemental composition (see Fig. 1(d)). The atomic percentage of the Sc dopants is calculated to be 11%, matching well with the nominal value of the sputtering target.

To assess the crystallinity and lattice structure information of the ScAlN sample, we compare it with a similarly sputtered undoped AlN thin film using X-ray diffraction (XRD) measurement (see Fig. 1(e)). Assignment of planes to peaks is based on the standard diffraction patterns of AlN from crystallographic data base. The X-ray wavelength from the synchrotron source is calibrated to be 0.154 nm with the substrate silicon (004) peak at  $2\theta = 69.09^\circ$ . The AlN data shows that it is single-phase with the  $c$ -axis perpendicular to the film surface. The AlN(0002) and AlN(0004) peaks at  $35.96^\circ$  and  $76.24^\circ$  correspond to higher order diffractions ( $n = 2, 4$ ), and the lattice parameter is calculated to be 0.4989 nm, agree-

ing well with the literature value of  $0.4980 \text{ nm}^{29}$ . The slight down-shift of the ScAlN(0002) and ScAlN(0004) peaks at  $35.84^\circ$  and  $75.96^\circ$  correspond to a slightly larger lattice parameter of  $0.5005 \text{ nm}$ , indicating a small expansion of lattice due to the larger ionic radius of  $\text{Sc}^{3+}$  than that of  $\text{Al}^{3+}$ . An additional peak at  $32.96^\circ$  is assigned to the first-order diffraction from the  $m$  plane (10-10). The corresponding lattice parameter is  $0.2715 \text{ nm}$  and the lattice constant is  $0.3135 \text{ nm}$ , slightly larger than the literature value of  $0.3110 \text{ nm}^{29}$ . This is again attributed to the larger ionic radius of  $\text{Sc}^{3+}$ . The presence of the  $m$  plane peak together with the dominant  $c$  plane peaks indicates that some parts of the film has the  $c$ -axis pointing in-plane, likely due to non-uniformity in the ScAlN film. The rocking curve measurements of the (0002) peaks (Fig. 1(e) inset) show a full-width at half-maximum (FWHM) of  $1.8^\circ$  for both doped and non-doped films. This value is consistent with other sputter-deposited AlN films in the literature<sup>30,31</sup>, but larger than those grown using epitaxial growth methods, whose rocking curve FWHM is as small as  $0.004^\circ$ <sup>32</sup>.

Next, we characterize the second-order nonlinear ( $\chi^{(2)}$ ) optical response of ScAlN using a second-harmonic generation (SHG) confocal microscope. The inset in Fig. 1(f) shows a simplified schematic of the measurement setup. A femtosecond pulsed laser at  $1030 \text{ nm}$  is focused on the target film through an objective lens. The SHG signal at  $515 \text{ nm}$  is collected through the same objective lens and directed to a silicon avalanche photo-detector (APD) using a dichroic mirror. Four different thin-film samples are measured: 10% doped ScAlN ( $\text{Sc}_{0.1}\text{Al}_{0.9}\text{N}$ ), 30% doped ScAlN ( $\text{Sc}_{0.3}\text{Al}_{0.7}\text{N}$ ), undoped AlN, and z-cut LN (shown in Fig. 1(f)). The  $\text{Sc}_{0.1}\text{Al}_{0.9}\text{N}$ ,  $\text{Sc}_{0.3}\text{Al}_{0.7}\text{N}$ , and AlN films are all  $500 \text{ nm}$  thick. The single-crystal z-cut LN film ( $600 \text{ nm}$ ) is used as a reference to calibrate the  $\chi^{(2)}$  values. The quadratic dependence of the SHG signals on the pump power is illustrated by the straight fitting lines. It is clear that the  $\chi^{(2)}$  nonlinearity of ScAlN increases with Sc doping concentration. The relevant  $\chi^{(2)}$  components for AlN and ScAlN are  $d_{33}$  and  $d_{31}$ . In our measurement configuration, most SHG signals originate from  $d_{31}$ . Using LN as a reference ( $d_{31} = 4.3 \text{ pm/V}^{33}$ ), we estimate  $d_{31} \simeq 0.2, 1.0$  and  $1.8 \text{ pm/V}$  for undoped AlN, 10% doped ScAlN, and 30% doped ScAlN, respectively. These numbers are on the same order of magnitude as literature values<sup>7,34–36</sup>, and the deviations might be caused by differences in film quality. During pump power sweep, we noticed that ScAlN films have higher damage thresholds than AlN, suggesting potentially higher power handling capability with doping.

After the material study, we fabricate waveguides and ring resonators with the 10% doped ScAlN and assess their losses. The ring radius is designed to be  $140 \mu\text{m}$  to reduce the bending loss. The ring and the bus waveguide widths are  $1.5 \mu\text{m}$  and  $800 \text{ nm}$ , respectively. A pulley coupling scheme with  $5^\circ$  coupling length is applied to extract the fundamental transverse-electric (TE) mode. The coupling gap between the ring and the bus waveguide is varied from  $300 \text{ nm}$  to  $1000 \text{ nm}$  to identify the critical coupling condition. Grating couplers are used to couple light between the waveguides and optical fibers. The devices are patterned using electron beam lithography (EBL) with hydrogen silsesquioxane (HSQ) resist. The

HSQ patterns are transferred to the ScAlN film using inductively coupled plasma-reactive ion etching (ICP-RIE) with chlorine chemistry, and the ScAlN films are fully etched to form ridge waveguides. With optimized ICP/RF powers and chamber pressure, the etch selectivity of HSQ to ScAlN is suppressed to  $<1$ , and we achieved smooth side wall without re-deposition. Finally, a layer of  $1.7 \mu\text{m}$   $\text{SiO}_2$  cladding is grown on top of the waveguide using plasma-enhanced chemical vapor deposition (PECVD).

Fig. 2(a) shows an optical microscope image of a typical ring resonator. Fig. 2(b) is an SEM image of the waveguide, showing a smooth side wall without re-deposition. Fig. 2(c) shows the grating coupler, designed to match  $8^\circ$  single-mode fiber array for TE mode coupling at  $1550 \text{ nm}$ . The waveguide cross-section is shown in Fig. 2(d). Fig. 2(e) is a magnified SEM of the waveguide cross-section (ScAlN marked purple, and unremoved HSQ marked cyan), showing a sidewall angle of  $70^\circ$ . We noticed some vertical strata in the ScAlN waveguide, which may suggest the existence of nanocolumns in the film. The inset shows a simulated fundamental TE mode, which is well confined inside the waveguide.

Fig. 3(a) shows a measured transmission spectrum of the ring resonator from  $1500 \text{ nm}$  to  $1630 \text{ nm}$ . The extinction ratio is close to  $20 \text{ dB}$  for most of the resonances, indicating that the resonator is close to critical coupling. Several groups of modes are observed. By extracting the group indices from the free spectral ranges (FSR), we identify three families of TE modes. Via fitting, we obtain an average intrinsic  $Q$  of the fundamental TE mode (TE0) of  $1.00 \times 10^5$ . Fig. 3(b) is the intrinsic  $Q$  distribution of the TE0 mode over the whole grating coupler pass band. The intrinsic  $Q$  for the higher-order TE modes (TE1, TE2) are around  $0.60 \times 10^5$ . This is because the higher order modes tend to experience larger interface scattering. Fig. 3(c) is a typical resonance near  $1550 \text{ nm}$  with an intrinsic  $Q$  of  $1.02 \times 10^5$ . A maximum intrinsic  $Q$  of  $1.47 \times 10^5$  is found in a similar device at longer wavelength (Fig. 3(d)). This corresponds to a propagation loss of  $2.4 \text{ dB/cm}$ .

### III. DISCUSSION

To improve the resonator  $Q$  and reduce loss, we have studied several loss-reduction methods during fabrication. Two major sources of loss are the scattering loss from the surface and the absorption loss due to material imperfection. We investigated the variation of the surface roughness with thickness removed through either dry etching or chemical mechanical polishing (CMP) in Fig. 4(a). The CMP method is more efficient in reducing the surface roughness and the final RMS surface roughness is reduced to  $<1 \text{ nm}$  with  $160 \text{ nm}$  of ScAlN polished away. However, the high- $Q$  devices shown in Fig. 3 are only polished down to  $400 \text{ nm}$ . This is to ensure the mode is mostly confined inside the ScAlN for a maximal confinement factor, which is desired in nonlinear optics applications. The material loss is reduced by annealing the device at high temperatures. Fig. 4(b) shows the changes of intrinsic  $Q$  at different annealing temperatures for 1 h annealing time. The optimal annealing temperature is  $400^\circ\text{C}$  for all TE modes. We observed that a longer annealing time was required for more densely written structures, suggesting the



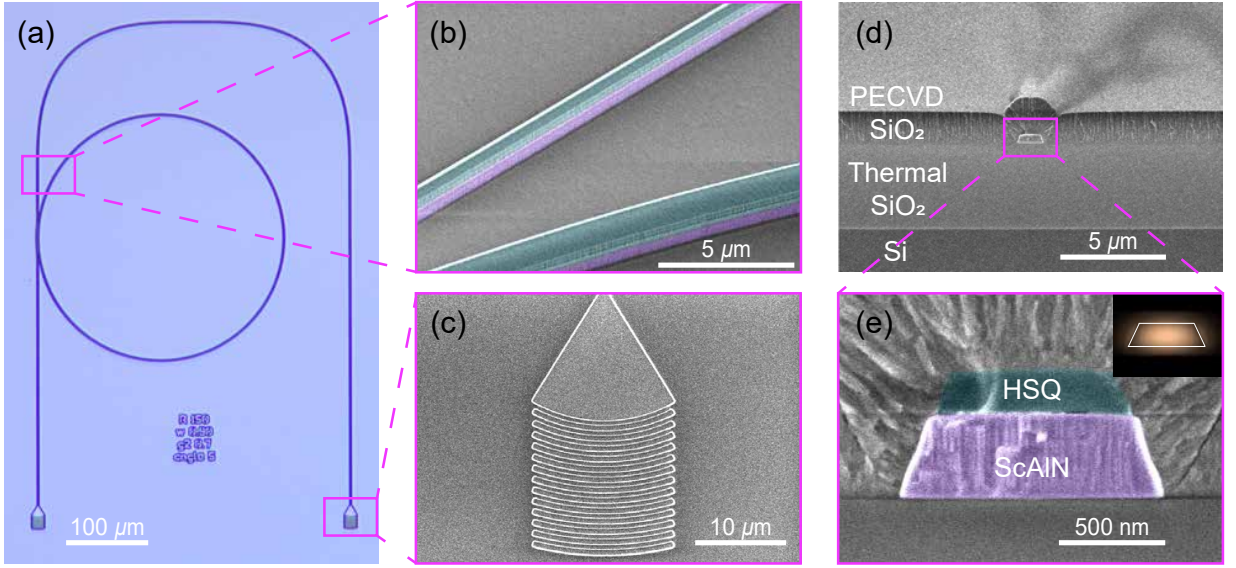


FIG. 2. ScAlN waveguides and ring resonators. (a) Optical microscope image of a typical ring resonator. The ring resonator is pulley-coupled to the bus waveguide. Light in the waveguide is coupled to single-mode fibers using grating couplers. (b) SEM image of ring-bus coupling region. The ScAlN waveguides are false-colored in purple and the HSQ resist is in cyan. (c) SEM image of the grating coupler. (d) SEM image of the waveguide cross-section. A  $1.7\ \mu\text{m}$ -thick PECVD oxide layer is deposited as a cladding. (e) Magnified view of the waveguide cross-section. Inset shows the simulated fundamental TE mode.

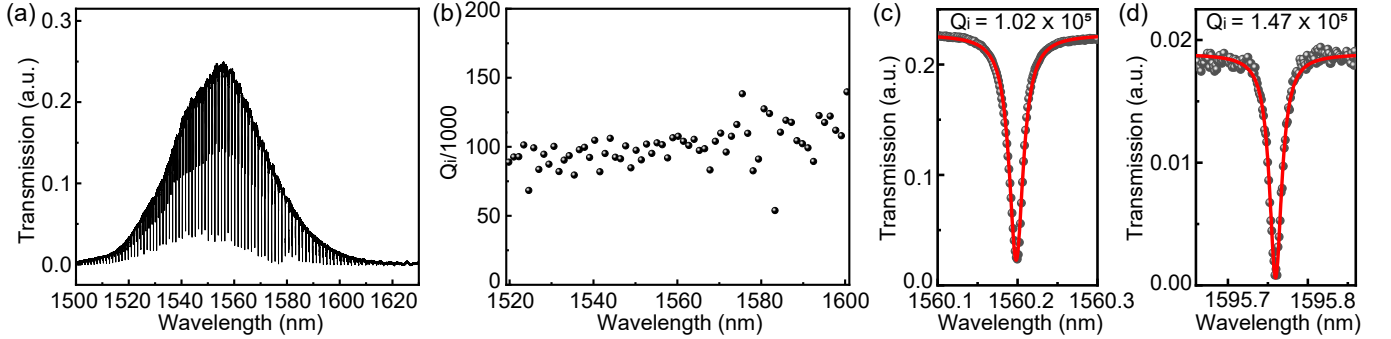


FIG. 3. Transmission measurement and  $Q$  factor extraction. (a) Transmission spectrum of a ring resonator with grating couplers. Multiple TE modes are observed. The fundamental TE mode is nearly critically coupled. (b) The average intrinsic  $Q$  factors of the fundamental TE mode is around  $Q = 1.00 \times 10^5$ . (c) A typical resonance with  $Q = 1.02 \times 10^5$ . (d) A resonance with an intrinsic  $Q = 1.47 \times 10^5$  is obtained in a similar device.

possibility of electron-beam damage in the material. Any further extension of annealing time does not deteriorate the  $Q$ . Two annealing gases, argon (Ar) and nitrogen ( $\text{N}_2$ ), are investigated, but we did not observe a significant difference in the  $Q$  factors obtained. Fig. 4(c) shows the representative resonances at different annealing temperatures and the corresponding intrinsic  $Q$  factors. After optimizing the surface roughness and the annealing temperature, the largest potential in improving  $Q$  is in reducing material absorption loss. There have been many efforts to vary the deposition conditions including deposition temperature, power, pressure, gas ratio and substrate<sup>19,37–41</sup> to improve the sputtering film quality. Despite the extended efforts, the sputtered ScAlN films generally exhibit a relatively wide rocking curve with a FWHM of  $>1^\circ$ . Hence, other growth techniques such as epitaxial growth with

molecular beam epitaxy (MBE)<sup>42,43</sup> and metal organic chemical vapor deposition (MOCVD)<sup>44</sup> are being investigated for growing high-quality ScAlN films with better crystallinity. An alternative way to avoid the material absorption is to push the mode outside of the waveguide at the expense of a reduction in mode overlap with the ScAlN waveguide. For example, a study on a 30% doped ScAlN thin film with 150 nm thickness has reported a propagation loss of 2.26 dB/cm from a race-track resonator measurement, and extracted the corresponding loss from the straight section of the racetrack resonator to be 1.6 dB/cm<sup>26</sup>.

#### IV. CONCLUSION

In summary, we have demonstrated the fabrication of low-loss waveguides and ring resonators on PVD-grown thin-film

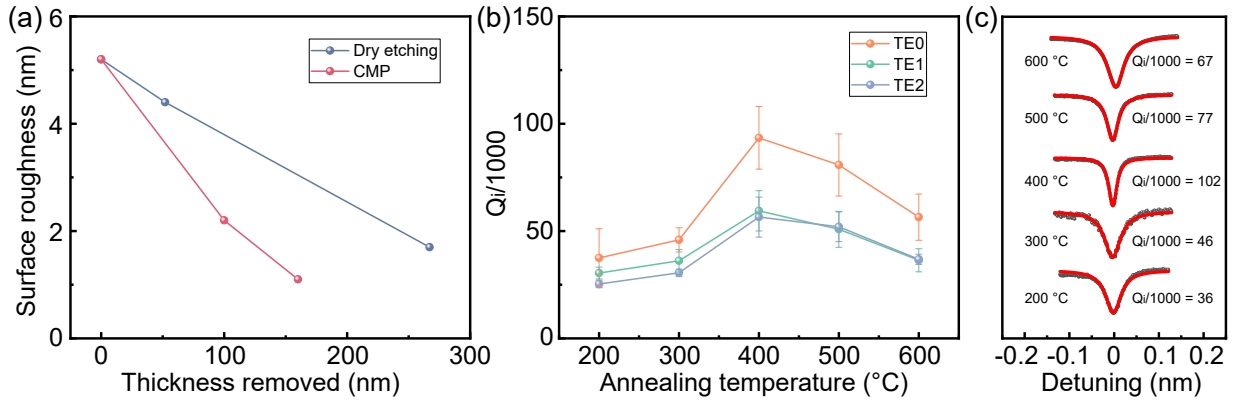


FIG. 4. Loss reduction investigation. (a) Surface roughness against thickness removed for two methods. CMP is more efficient in smoothing the film surface. (b) Intrinsic  $Q$  factors as a function of annealing temperatures, revealing an optimal annealing temperature of 400 °C. (c) Typical resonances of TE0 mode at different annealing temperatures.

ScAlN. The highest measured intrinsic  $Q$  is  $1.47 \times 10^5$ , corresponding to a propagation loss of 2.4 dB/cm. A dry etching recipe based on chlorine chemistry is developed to achieve a fully etched structure with a smooth, redeposition-free sidewall. We identified an optimal annealing temperature of 400 °C for reducing the waveguide loss. Our results serve as an important step towards future large-scale photonic integrated circuits on thin-film ScAlN. Currently, the dominant loss is still from material imperfections, which may be improved through further optimizations in deposition processes to achieve better crystallinity and homogeneity. Future developments of functional devices beyond linear components, such as electro-optic modulators, acousto-optic modulators, and various nonlinear optical devices, are the immediate next steps to unlock the full potential of this material platform.

## V. ACKNOWLEDGEMENT

This work is supported by A\*STAR (C230917005 for device fabrication and measurement, C220415015 for ScAlN thin film deposition, and M23M5a0069 for ScAlN characterization and results analysis) and National Research Foundation (NRF2022-QEP2-01-P07, NRF-NRFF15-2023-0005, NRF-CRP28-2022-0002). The authors would like to thank Jie Deng, Seng Kai Wong, Sherry Yap, Aihong Huang and Qingxin Zhang for assistance in device fabrication; Ming Lu and Jiapeng Sun for assistance in manuscript preparation. The fabrication of the devices was done at the A\*STAR Cleanroom.

## VI. AUTHOR DECLARATIONS

The authors have no conflicts to disclose.

## REFERENCES

- <sup>1</sup>M. Smit, K. Williams, and J. Van Der Tol, "Past, present, and future of InP-based photonic integration," *APL Photonics* **4**, 050901 (2019).
- <sup>2</sup>C. Xiang, S. M. Bowers, A. Bjorlin, R. Blum, and J. E. Bowers, "Perspective on the future of silicon photonics and electronics," *Applied Physics Letters* **118**, 220501 (2021).
- <sup>3</sup>Y. Shen, N. C. Harris, S. Skirlo, M. Prabhu, T. Baehr-Jones, M. Hochberg, X. Sun, S. Zhao, H. Larochelle, D. Englund, *et al.*, "Deep learning with coherent nanophotonic circuits," *Nature Photonics* **11**, 441–446 (2017).
- <sup>4</sup>X. Zhang, K. Kwon, J. Henriksson, J. Luo, and M. C. Wu, "A large-scale microelectromechanical-systems-based silicon photonics lidar," *Nature* **603**, 253–258 (2022).
- <sup>5</sup>Z. L. Newman, V. Maurice, T. Drake, J. R. Stone, T. C. Briles, D. T. Spencer, C. Fredrick, Q. Li, D. Westly, B. R. Ilic, B. Shen, M.-G. Suh, K. Y. Yang, C. Johnson, D. M. S. Johnson, L. Hollberg, K. J. Vahala, K. Srinivasan, S. A. Diddams, J. Kitching, S. B. Papp, and M. T. Hummon, "Architecture for the photonic integration of an optical atomic clock," *Optica* **6**, 680–685 (2019).
- <sup>6</sup>M.-G. Suh, Q.-F. Yang, K. Y. Yang, X. Yi, and K. J. Vahala, "Microresonator soliton dual-comb spectroscopy," *Science* **354**, 600–603 (2016).
- <sup>7</sup>N. Li, C. P. Ho, S. Zhu, Y. H. Fu, Y. Zhu, and L. Y. T. Lee, "Aluminum nitride integrated photonics: a review," *Nanophotonics* **10**, 2347–2387 (2021).
- <sup>8</sup>J. P. Kar and G. Bose, "Aluminum nitride (AlN) film based acoustic devices: material synthesis and device fabrication," *Acoustic Waves-From Microdevices to Helioseismology*, InTech, 563 (2011).
- <sup>9</sup>C. Xiong, W. H. Pernice, X. Sun, C. Schuck, K. Y. Fong, and H. X. Tang, "Aluminum nitride as a new material for chip-scale optomechanics and nonlinear optics," *New Journal of Physics* **14**, 095014 (2012).
- <sup>10</sup>A. W. Bruch, X. Liu, Z. Gong, J. B. Surya, M. Li, C.-L. Zou, and H. X. Tang, "Pockels soliton microcomb," *Nature Photonics* **15**, 21–27 (2021).
- <sup>11</sup>J. Edgar, Z. Yu, A. Ahmed, and A. Rys, "Low temperature metal-organic chemical vapor deposition of aluminum nitride with nitrogen trifluoride as the nitrogen source," *Thin Solid Films* **189**, L11–L14 (1990).
- <sup>12</sup>T.-J. Lu, M. Fanto, H. Choi, P. Thomas, J. Steidle, S. Mouradian, W. Kong, D. Zhu, H. Moon, K. Berggren, *et al.*, "Aluminum nitride integrated photonics platform for the ultraviolet to visible spectrum," *Optics Express* **26**, 11147–11160 (2018).
- <sup>13</sup>X. Liu, A. W. Bruch, and H. X. Tang, "Aluminum nitride photonic integrated circuits: from piezo-optomechanics to nonlinear optics," *Advances in Optics and Photonics* **15**, 236–317 (2023).
- <sup>14</sup>N. Kerness, T. Hossain, and S. McGuire, "Impurity study of alumina and aluminum nitride ceramics: Microelectronics packaging applications," *Applied Radiation and Isotopes* **48**, 5–9 (1997).
- <sup>15</sup>N. Takeuchi, "First-principles calculations of the ground-state properties and stability of ScN," *Physical Review B* **65**, 045204 (2002).
- <sup>16</sup>N. Farrer and L. Bellaiche, "Properties of hexagonal ScN versus wurtzite GaN and InN," *Physical Review B* **66**, 201203 (2002).
- <sup>17</sup>V. Ranjan, S. Bin-Omran, D. Sichuga, R. S. Nichols, L. Bellaiche, and A. Alsaad, "Properties of GaN/ScN and InN/ScN superlattices from first principles," *Physical Review B* **72**, 085315 (2005).
- <sup>18</sup>A. Alsaad and A. Ahmad, "Piezoelectricity of ordered (Sc<sub>x</sub>Ga<sub>1-x</sub>)N alloys from first principles," *The European Physical Journal B-Condensed Matter and Complex Systems* **54**, 151–156 (2006).
- <sup>19</sup>M. Akiyama, T. Kamohara, K. Kano, A. Teshigahara, Y. Takeuchi, and

- N. Kawahara, "Enhancement of piezoelectric response in scandium aluminum nitride alloy thin films prepared by dual reactive cosputtering," *Advanced Materials* **21**, 593–596 (2009).
- <sup>20</sup>S. Fichtner, N. Wolff, F. Lofink, L. Kienle, and B. Wagner, "AlScN: A iii-v semiconductor based ferroelectric," *Journal of Applied Physics* **125** (2019).
- <sup>21</sup>F. Yang, G. Yang, D. Wang, P. Wang, J. Lu, Z. Mi, and H. X. Tang, "Domain control and periodic poling of epitaxial ScAlN," *Applied Physics Letters* **123**, 101103 (2023).
- <sup>22</sup>P. Wang, D. Wang, S. Mondal, M. Hu, J. Liu, and Z. Mi, "Dawn of nitride ferroelectric semiconductors: from materials to devices," *Semiconductor Science and Technology* **38**, 043002 (2023).
- <sup>23</sup>V. Yoshioka, J. Lu, Z. Tang, J. Jin, R. H. Olsson, and B. Zhen, "Strongly enhanced second-order optical nonlinearity in cmos-compatible  $\text{Al}_{1-x}\text{Sc}_x\text{N}$  thin films," *APL Materials* **9**, 101104 (2021).
- <sup>24</sup>S. Zhu, Q. Zhong, N. Li, T. Hu, Y. Dong, Z. Xu, Y. Zhou, Y. H. Fu, and N. Singh, "Integrated ScAlN photonic circuits on silicon substrate," in *Conference on Lasers and Electro-Optics* (Optica Publishing Group, 2020) p. STu3P.5.
- <sup>25</sup>J. Liu, W. Shin, P. Wang, D. Wang, M. Soltani, and Z. Mi, "Ferroelectric ScAlN: Epitaxy, properties, and emerging photonic device applications," in *2022 IEEE Photonics Conference (IPC)* (IEEE, 2022) pp. 1–2.
- <sup>26</sup>B. Friedman, S. Barth, T. Schreiber, H. Bartsch, J. Bain, and G. Piazza, "Measured optical losses of Sc doped AlN waveguides," *Optics Express* **32**, 5252–5260 (2024).
- <sup>27</sup>S. Zhang, D. Holec, W. Y. Fu, C. J. Humphreys, and M. A. Moram, "Tunable optoelectronic and ferroelectric properties in Sc-based iii-nitrides," *Journal of Applied Physics* **114**, 133510 (2013).
- <sup>28</sup>J. M. Wall and F. Yan, "Sputtering process of  $\text{Sc}_x\text{Al}_{1-x}\text{N}$  thin films for ferroelectric applications," *Coatings* **13**, 54 (2022).
- <sup>29</sup>H. Schulz and K. Thiemann, "Crystal structure refinement of aln and gan," *Solid State Communications* **23**, 815–819 (1977).
- <sup>30</sup>C. Xiong, W. H. Pernice, and H. X. Tang, "Low-loss, silicon integrated, aluminum nitride photonic circuits and their use for electro-optic signal processing," *Nano Letters* **12**, 3562–3568 (2012).
- <sup>31</sup>A. Iqbal and F. Mohd-Yasin, "Reactive sputtering of aluminum nitride (002) thin films for piezoelectric applications: A review," *Sensors* **18**, 1797 (2018).
- <sup>32</sup>Z. Zhang, Y. Hayashi, T. Tohei, A. Sakai, V. Protasenko, J. Singhal, H. Miyake, H. G. Xing, D. Jena, and Y. Cho, "Molecular beam homoepitaxy of N-polar AlN: Enabling role of aluminum-assisted surface cleaning," *Science Advances* **8**, eabo6408 (2022).
- <sup>33</sup>D. Zhu, L. Shao, M. Yu, R. Cheng, B. Desiatov, C. Xin, Y. Hu, J. Holzgrafe, S. Ghosh, A. Shams-Ansari, *et al.*, "Integrated photonics on thin-film lithium niobate," *Advances in Optics and Photonics* **13**, 242–352 (2021).
- <sup>34</sup>G. Kiehne, G. Wong, and J. Ketterson, "Optical second-harmonic generation in sputter-deposited AlN films," *Journal of Applied Physics* **84**, 5922–5927 (1998).
- <sup>35</sup>A. Majkić, A. Franke, R. Kirste, R. Schlessler, R. Collazo, Z. Sitar, and M. Zgonik, "Optical nonlinear and electro-optical coefficients in bulk aluminium nitride single crystals," *Physica Status Solidi (b)* **254**, 1700077 (2017).
- <sup>36</sup>X. Liu, A. W. Bruch, and H. X. Tang, "AlN nonlinear optics and integrated photonics," *Semiconductors and Semimetals* **107**, 223–281 (2021).
- <sup>37</sup>M. Akiyama, K. Kano, and A. Teshigahara, "Influence of growth temperature and scandium concentration on piezoelectric response of scandium aluminum nitride alloy thin films," *Applied Physics Letters* **95**, 162107 (2009).
- <sup>38</sup>J. Tang, D. Niu, Z. Tai, and X. Hu, "Deposition of highly c-axis-oriented ScAlN thin films at different sputtering power," *Journal of Materials Science: Materials in Electronics* **28**, 5512–5517 (2017).
- <sup>39</sup>S. Fichtner, T. Reimer, S. Chemnitz, F. Lofink, and B. Wagner, "Stress controlled pulsed direct current co-sputtered  $\text{Al}_{1-x}\text{Sc}_x\text{N}$  as piezoelectric phase for micromechanical sensor applications," *APL Materials* **3**, 116102 (2015).
- <sup>40</sup>Y. Zhang, W. Zhu, D. Zhou, Y. Yang, and C. Yang, "Effects of sputtering atmosphere on the properties of c-plane ScAlN thin films prepared on sapphire substrate," *Journal of Materials Science: Materials in Electronics* **26**, 472–478 (2015).
- <sup>41</sup>C. Höglund, J. Birch, B. Alling, J. Bareño, Z. Czigány, P. O. Persson, G. Wingqvist, A. Zukauskaitė, and L. Hultman, "Wurtzite structure  $\text{Sc}_{1-x}\text{Al}_x\text{N}$  solid solution films grown by reactive magnetron sputter epitaxy: Structural characterization and first-principles calculations," *Journal of Applied Physics* **107**, 123515 (2010).
- <sup>42</sup>M. T. Hardy, B. P. Downey, N. Nepal, D. F. Storm, D. S. Katzer, and D. J. Meyer, "Epitaxial ScAlN grown by molecular beam epitaxy on GaN and SiC substrates," *Applied Physics Letters* **110**, 162104 (2017).
- <sup>43</sup>D. Wang, P. Wang, S. Mondal, J. Liu, M. Hu, M. He, S. Nam, W. Peng, S. Yang, D. Wang, *et al.*, "Controlled ferroelectric switching in ultrawide bandgap AlN/ScAlN multilayers," *Applied Physics Letters* **123**, 103506 (2023).
- <sup>44</sup>S. Leone, J. Ligl, C. Manz, L. Kirste, T. Fuchs, H. Menner, M. Prescher, J. Wiegert, A. Žukauskaitė, R. Quay, *et al.*, "Metal-organic chemical vapor deposition of aluminum scandium nitride," *Physica Status Solidi (RRL)–Rapid Research Letters* **14**, 1900535 (2020).